Spectral Quadrature method for accurate $\mathcal{O}(N)$ electronic structure calculations of metals and insulators

Phanisri P. Pratapa[a], Phanish Suryanarayana[*,a], John E. Pask[b]

[a] *College of Engineering, Georgia Institute of Technology, Atlanta, GA 30332, USA*
[b] *Physics Division, Lawrence Livermore National Laboratory, Livermore, CA 94550, USA*

Abstract

We present the Clenshaw-Curtis Spectral Quadrature (SQ) method for real-space $\mathcal{O}(N)$ Density Functional Theory (DFT) calculations. In this approach, all quantities of interest are expressed as bilinear forms or sums over bilinear forms, which are then approximated by spatially localized Clenshaw-Curtis quadrature rules. This technique is identically applicable to both insulating and metallic systems, and in conjunction with local reformulation of the electrostatics, enables the $\mathcal{O}(N)$ evaluation of the electronic density, energy, and atomic forces. The SQ approach also permits infinite-cell calculations without recourse to Brillouin zone integration or large supercells. We employ a finite difference representation in order to exploit the locality of electronic interactions in real space, enable systematic convergence, and facilitate large-scale parallel implementation. In particular, we derive expressions for the electronic density, total energy, and atomic forces that can be evaluated in $\mathcal{O}(N)$ operations. We demonstrate the systematic convergence of energies and forces with respect to quadrature order as well as truncation radius to the exact diagonalization result. In addition, we show convergence with respect to mesh size to established $\mathcal{O}(N^3)$ planewave results. Finally, we establish the efficiency of the proposed approach for high temperature calculations and discuss its particular suitability for large-scale parallel computation.

Key words: Density Functional Theory; Spectral quadrature; Clenshaw-Curtis; Linear-scaling; Metallic systems; Atomic forces

1. Introduction

Over the course of the past few decades, the Density Functional Theory (DFT) of Hohenberg, Kohn, and Sham [1, 2] has been widely employed for understanding and predicting a wide range of materials properties, from the first principles of quantum mechanics, with no empirical or adjustable parameters. The tremendous popularity of DFT stems from its high accuracy to cost ratio when compared to other such ab initio theories. However, the solution of the required Kohn-Sham equations—with Schrödinger type three-dimensional eigenproblem for the orbitals [3]—remains a formidable task. This has severely limited the range of physical systems accessible to such quantum mechanical investigation, with routine calculations limited to a few hundred atoms or less.

The main computational bottleneck in DFT calculations is the solution of the Kohn-Sham eigenproblem for the eigenfunctions and corresponding eigenvalues. The number of eigenfunctions that need to be calculated is proportional to the number of atoms in the system N. Since the eigenfunctions need to be

*Corresponding Author (*phanish.suryanarayana@ce.gatech.edu*)

orthogonal, the overall computational complexity of DFT calculations is $\mathcal{O}(N^3)$ [4, 5]. This orthogonality constraint also results in global communications between processors in parallel computations, limiting parallel scalability. The need for high performance parallel computing is especially acute in the context of ab initio molecular dynamics [6, 7], wherein the Kohn-Sham equations must be solved at each molecular dynamics time step, thereby requiring tens to hundreds of thousands of force evaluations to complete a single simulation.

To overcome the critical $\mathcal{O}(N^3)$ scaling bottleneck, much work has been done in the past two decades to develop solution strategies that scale linearly with the number of atoms, i.e., $\mathcal{O}(N)$ (see, e.g., [8, 9] and references therein). These methods eliminate the computation of the Kohn-Sham orbitals, proceeding instead directly from Hamiltonian to density and total energy without diagonalization. Mature codes are now available implementing a number of the key ideas [10, 11, 12, 13, 14, 15, 16, 17, 18, 19, 20, 21, 22]. However, despite steady and substantial advances, significant challenges remain. Accuracy and stability of $\mathcal{O}(N)$ approaches remain ongoing concerns due to the need for additional computational parameters, subtleties in determining sufficient numbers and/or centers of localized orbitals, and limitations of underlying basis sets, among others [9]. In real-space representations, the calculation of accurate atomic forces, as required for structural relaxations and molecular dynamics, has been a particular concern in $\mathcal{O}(N)$ as well as $\mathcal{O}(N^3)$ scaling methods [23, 24]. Perhaps most importantly, due to the assumption of a band gap in the electronic structure, the application of existing methods to metallic systems remains an open question [9]. Furthermore, due to the complex communications patterns and load balance issues which arise, particularly in localized orbital formulations, efficient large-scale parallelization poses a significant challenge.

The Spectral Quadrature (SQ) method has been recently proposed for the $\mathcal{O}(N)$ solution of the Kohn-Sham equations [25]. In SQ, the required electronic density, energy, and atomic forces are expressed as integrals over projected densities of states and related quantities. With the choice of Gauss quadrature for integration, the method becomes equivalent to the classical recursion method [26, 27], while for Clenshaw-Curtis quadrature, the Fermi operator expansion (FOE) [28, 29] in Chebyshev polynomials is recovered. Since no assumption is made regarding the presence or absence of a band gap in the electronic structure, the SQ approach is general and applicable to metals and insulators alike. The computational cost of SQ is, however, inversely proportional to temperature, whereby it has a larger prefactor for metallic systems at lower temperature. Nevertheless, the amenability of SQ to large-scale parallel computation (Section 5.4) stands to mitigate this cost.

In this work, we focus on the Clenshaw-Curtis variant of SQ since the atomic forces can be efficiently calculated compared to Gauss SQ. Moreover, the need for orthogonalization in Gauss SQ can limit performance when high orders of quadrature are required due to large spectral widths of the Hamiltonian. We develop a finite difference representation of this approach in order to exploit the locality of electronic interactions in real space, enable systematic convergence, and facilitate large-scale parallel implementation. In particular, we derive expressions for the electronic density, total energy, and atomic forces that can be evaluated in $\mathcal{O}(N)$ operations. We demonstrate the systematic convergence of energies and forces with respect to quadrature order and truncation radius to the exact diagonalization result, as well as convergence with mesh size to established $\mathcal{O}(N^3)$ scaling planewave results. We also show the efficiency of the proposed approach for high temperature calculations and discuss its particular suitability for large-scale parallel computation.

The remainder of this paper is organized as follows. In Section 2, we review the $\mathcal{O}(N)$ formulation of DFT in terms of the density matrix. We then present the $\mathcal{O}(N)$ Clenshaw-Curtis SQ electronic structure method in Section 3, and its numerical implementation in Section 4. Next, we present results for selected test cases and discuss large-scale parallel implementation in Section 5. Finally, we provide concluding remarks in Section 6.

2. $\mathcal{O}(N)$ Density Functional Theory

Consider a system of N atoms with a total of N_e valence electrons in a cuboidal domain Ω under periodic boundary conditions. Let the nuclei be at positions $\mathbf{R} = \{\mathbf{R}_1, \mathbf{R}_2, \ldots, \mathbf{R}_N\}$ and possess charges $\{Z_1, Z_2, \ldots, Z_N\}$, respectively. Neglecting spin, the system's free energy in Density Functional Theory (DFT) is of the form [30]

$$\mathcal{F}(\mathcal{D}, \mathbf{R}) = 2\mathrm{Tr}\left(-\frac{1}{2}\nabla^2\mathcal{D}\right) + E_{xc}(\rho_{\mathcal{D}}) + 2\mathrm{Tr}(\mathcal{V}_{nl}\mathcal{D}) + E_{el}(\rho_{\mathcal{D}}, \mathbf{R}) - T\mathcal{S}(\mathcal{D})\,, \tag{1}$$

where $\mathrm{Tr}(.)$ denotes the trace, $\mathcal{D}$ is the density operator, $\mathcal{V}_{nl}$ is the nonlocal pseudopotential operator, T is the electronic temperature, and the electron density

$$\rho_{\mathcal{D}}(\mathbf{x}) = 2\mathcal{D}(\mathbf{x}, \mathbf{x})\,. \tag{2}$$

The first term in Eqn. 1 corresponds to the kinetic energy of the non-interacting electrons, the second term is the exchange-correlation energy, the third term is the nonlocal pseudopotential energy, and the fourth term is the electrostatic energy. The final term gives the contribution arising from the electronic entropy:

$$\mathcal{S}(\mathcal{D}) = -2k_B\mathrm{Tr}\left(\mathcal{D}\log\mathcal{D} + (\mathcal{I} - \mathcal{D})\log(\mathcal{I} - \mathcal{D})\right)\,, \tag{3}$$

where k_B is the Boltzmann constant, and $\mathcal{I}$ is the identity operator.

We utilize the Local Density Approximation (LDA) [2] for the exchange-correlation energy:

$$E_{xc}(\rho_{\mathcal{D}}) = \int_{\Omega} \varepsilon_{xc}(\rho_{\mathcal{D}}(\mathbf{x}))\rho_{\mathcal{D}}(\mathbf{x})\,\mathrm{d}\mathbf{x}\,, \tag{4}$$

where $\varepsilon_{xc}(\rho_{\mathcal{D}})$ is the sum of the exchange and correlation energy per particle of a uniform electron gas. For the nonlocal pseudopotential, we utilize the Kleinman-Bylander form [31]:

$$\mathcal{V}_{nl} = \sum_I \mathcal{V}_{nl}^I = \sum_I \sum_{lm} \gamma_l^I \left|\chi_{lm}^I\right\rangle \left\langle\chi_{lm}^I\right|\,, \tag{5}$$

where χ_{lm}^I are the projection functions, with l and m representing the azimuthal and magnetic quantum numbers, respectively. The summation index I runs over all atoms in Ω.

We employ a local reformulation of the electrostatic energy [32]:

$$\begin{aligned} E_{el}(\rho_{\mathcal{D}}, \mathbf{R}) &= \sup_{\phi}\left\{-\frac{1}{8\pi}\int_{\Omega}|\nabla\phi(\mathbf{x}, \mathbf{R})|^2\,\mathrm{d}\mathbf{x} + \int_{\Omega}(\rho_{\mathcal{D}}(\mathbf{x}) + b(\mathbf{x}, \mathbf{R}))\phi(\mathbf{x}, \mathbf{R})\,\mathrm{d}\mathbf{x}\right\} \\ &- \frac{1}{2}\sum_J \int_{\Omega} b_J(\mathbf{x}, \mathbf{R}_J)V_J(\mathbf{x}, \mathbf{R}_J)\,\mathrm{d}\mathbf{x} + \mathcal{E}_c(\mathbf{R})\,, \end{aligned} \tag{6}$$

where $\phi(\mathbf{x}, \mathbf{R})$ is the electrostatic potential [33], $b_J(\mathbf{x}, \mathbf{R}_J)$ is the charge density of the J^{th} nucleus that generates the potential $V_J(\mathbf{x}, \mathbf{R}_J)$ [34], $b(\mathbf{x}, \mathbf{R}) = \sum_J b_J(\mathbf{x}, \mathbf{R}_J)$ is the total charge density of the nuclei, and the summation index J runs over all the atoms in Ω and its periodic images in $\mathbb{R}^3$. The second to last term in Eqn. 6 represents the self energy of the nuclei [34, 35], and the last term—whose expression is presented in Appendix A—accounts for overlapping charge densities [32].

For a given configuration of nuclei, the ground-state density operator can be written as the solution of the constrained minimization problem [30, 5]

$$\mathcal{D}^* = \left\{ \arg\inf_{\mathcal{D}} \mathcal{F}(\mathcal{D}, \mathbf{R}) \quad \text{s.t.} \quad 2\mathrm{Tr}(\mathcal{D}) = N_e \right\} . \tag{7}$$

The corresponding Euler-Lagrange equation is a nonlinear fixed-point problem:

$$\mathcal{D} = g(\mathcal{H}, \mu, \sigma) = \left(1 + \exp\left(\frac{\mathcal{H} - \mu\mathcal{I}}{\sigma} \right) \right)^{-1} , \tag{8}$$

where $\sigma = k_B T$ is the smearing, the Fermi energy μ is the Lagrange multiplier used to enforce the constraint on number of electrons, and the Hamiltonian

$$\mathcal{H} = -\frac{1}{2}\nabla^2 + V_{xc} + \phi + \mathcal{V}_{nl} . \tag{9}$$

In the above expression, $V_{xc} = \delta E_{xc}/\delta\rho_{\mathcal{D}}$ is the exchange-correlation potential and ϕ is the solution of the Poisson equation

$$-\frac{1}{4\pi}\nabla^2\phi(\mathbf{x}, \mathbf{R}) = \rho_{\mathcal{D}}(\mathbf{x}) + b(\mathbf{x}, \mathbf{R}) \tag{10}$$

subject to periodic boundary conditions. The resulting density matrix has exponential decay in real-space for insulators as well as metallic systems at finite temperature [36, 37], a key property exploited by $\mathcal{O}(N)$ electronic structure methods.

Once the self-consistent problem in Eqn. 8 has been solved, the electronic ground-state free energy can be written as

$$\begin{aligned} \mathcal{F}_0(\mathbf{R}) \;=\; & 2\mathrm{Tr}(\mathcal{D}^*\mathcal{H}^*) + E_{xc}(\rho_{\mathcal{D}^*}) + \frac{1}{2}\int_\Omega (b(\mathbf{x}, \mathbf{R}) - \rho_{\mathcal{D}^*}(\mathbf{x}))\phi^*(\mathbf{x}, \mathbf{R})\,\mathrm{d}\mathbf{x} \\ & - \int_\Omega V_{xc}(\rho_{\mathcal{D}^*}(\mathbf{x}))\rho_{\mathcal{D}^*}(\mathbf{x})\,\mathrm{d}\mathbf{x} - \frac{1}{2}\sum_J \int_\Omega b_J(\mathbf{x}, \mathbf{R}_J) V_{\mathrm{loc}}^J(\mathbf{x}, \mathbf{R}_J)\,\mathrm{d}\mathbf{x} + \mathcal{E}_c(\mathbf{R}) \\ & + 2\sigma\mathrm{Tr}\left(\mathcal{D}^*\log\mathcal{D}^* + (\mathcal{I} - \mathcal{D}^*)\log(\mathcal{I} - \mathcal{D}^*)\right) , \end{aligned} \tag{11}$$

where $\mathcal{H}^*$ and ϕ^* are as in Eqns. 9 and 10 with $\rho_{\mathcal{D}} = \rho_{\mathcal{D}^*}$. The superscript '*' is used to denote quantities at the electronic ground state. Thereafter, the force on the I^{th} nucleus may be obtained as

$$\begin{aligned} \mathbf{f}_I \;=\; & -\frac{\partial\mathcal{F}_0(\mathbf{R})}{\partial\mathbf{R}_I} \\ =\; & \sum_{I'}\int_\Omega \nabla b_{I'}(\mathbf{x}, \mathbf{R}_{I'})(\phi^*(\mathbf{x}, \mathbf{R}) - V_{I'}(\mathbf{x}, \mathbf{R}_{I'}))\,\mathrm{d}\mathbf{x} + \mathbf{f}_I^c - 2\mathrm{Tr}\left[\mathcal{D}^*\frac{\partial\mathcal{V}_{nl}}{\partial\mathbf{R}_I}\right] , \end{aligned} \tag{12}$$

where the summation index I' runs over the I^{th} atom and its periodic images. In the above, $\mathbf{f}_I^c$ is the correction due to overlapping nuclear charge densities ($\mathbf{f}_I^c \equiv \mathbf{0}$ for no overlap) [32], the expression for which is presented in Appendix A.

The density matrix formulation of DFT as above corresponds to periodic boundary conditions on the unit cell Ω. For sufficiently large Ω (a few hundred to thousand atoms, depending on physical system), these boundary conditions suffice to obtain the infinite-crystal result, corresponding to repetition of Ω over all space. However, for less complex systems (e.g., elemental solids or compounds) with fewer atoms

in Ω, periodic boundary conditions are not sufficient. In such cases, the standard approach is to employ Bloch boundary conditions, whereby the desired infinite-crystal result can be obtained as an integral over the Brillouin zone [4]. However, this requires a separate Kohn-Sham calculation for each Bloch wavevector (k-point) in the integration, which can increase cost substantially. For example, metallic systems with small Ω at high pressure can require thousands of k-points to converge. The alternative in such a case would be a periodic calculation on a cell containing thousands of atoms, which for standard diagonalization based approaches would be prohibitive. Since the computational cost for such methods increases cubically with the number of atoms but only linearly with the number of k-points, computation on the small cell with integration over the Brillouin zone is generally the less costly alternative. As we show below, however, by exploiting the decay of the density matrix in real-space, the Spectral Quadrature method can in fact obtain the infinite-crystal result directly, without recourse to either large supercells or Brillouin zone integration.

3. Clenshaw-Curtis Spectral Quadrature Method

In this section, we discuss the Clenshaw-Curtis variant of the Spectral Quadrature (SQ) method [25]. We do so in the context of the finite-difference representation, a commonly used discretization scheme in electronic structure calculations [38, 39]. We employ the Self-Consistent Field (SCF) iteration [40, 41], wherein the electron density is iterated to the ground state (fixed point), after which total energy and atomic forces are computed. In this setting, we express all quantities of interest as bilinear forms, or sums over bilinear forms, and then approximate them using Clenshaw-Curtis quadrature rules.

3.1. Preliminaries

In view of the nearsightedness principle [42], we define the *region of influence* of any point in space as the cube of side $2R_{cut}$ centered at that point. We choose a cube rather than a sphere for simplicity and efficiency within the finite-difference discretization. The parameter R_{cut} corresponds to the truncation radius of the density matrix, the distance beyond which electronic interactions can be ignored. Indeed, the magnitude of the electronic interactions decreases exponentially with distance for insulators as well as metallic systems at finite temperature. We exploit this decay to perform $\mathcal{O}(N)$ Γ-point (periodic) calculations as well as infinite-cell (infinite-crystal) calculations.

Domain, discretization, and boundary conditions. We distinguish between Γ-point and infinite-cell calculations in the choice of domain and prescribed boundary conditions. For Γ-point calculations, we impose periodic boundary conditions on Ω, as shown in Fig. 1a. For infinite-cell calculations, we periodically extend Ω to Ω' and impose zero Dirichlet boundary conditions on Ω' for the Hamiltonian, as shown in Fig. 1b. However, we retain periodic boundary conditions on Ω for the Poisson problem. The size of Ω' is chosen such that it encompasses the region of influence of all finite-difference nodes in Ω. In this setting, we denote the discrete Hamiltonian, nonlocal pseudopotential matrix due to the I^{th} atom, and gradient by $\mathbf{H} \in \mathbb{R}^{N_d \times N_d}$, $\mathbf{V}_{nl}^{I} \in \mathbb{R}^{N_d \times N_d}$, and $\tilde{\nabla}_h \equiv (\nabla_{xh} \in \mathbb{R}^{N_d \times N_d}, \nabla_{yh} \in \mathbb{R}^{N_d \times N_d}, \nabla_{zh} \in \mathbb{R}^{N_d \times N_d})$, respectively. Here, N_d denotes the number of finite-difference nodes used to discretize Ω and Ω' in Γ-point and infinite-cell calculations, respectively, and h represents the finite-difference mesh size.

Nodal quantities. Let K_Ω denote the collection of finite-difference nodes used to discretize Ω. The nodal Hamiltonian $\mathbf{H}_p \in \mathbb{R}^{N_s \times N_s}$ of any node $p \in K_\Omega$ is defined as the restriction of the Hamiltonian to its region of influence:

$$\mathbf{H}_p = \mathbf{P}^T \mathbf{H} \mathbf{P} \,, \tag{13}$$

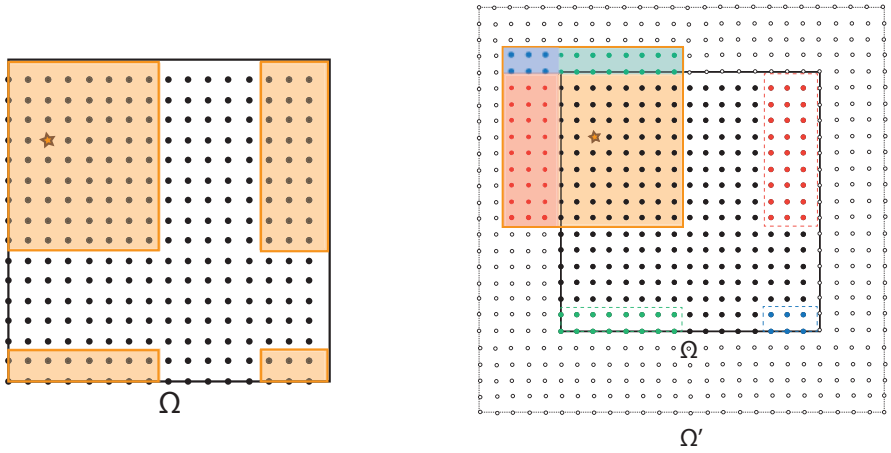

(a) Γ-point calculation (b) Infinite-cell calculation

Figure 1: Simulation domains and discretization used for Γ-point and infinite-cell calculations. Finite-difference nodes are represented by circles, with the shaded part defining the region of influence for the finite-difference node represented by the star. Periodic and zero Dirichlet boundary conditions are prescribed on Ω and Ω', respectively.

where the matrix

$$\mathbf{P} = \left[\mathbf{v}_{p_1}, \mathbf{v}_{p_2}, \ldots, \mathbf{v}_{p_{N_s}}\right] \in \mathbb{R}^{N_d \times N_s} . \tag{14}$$

Above, $\{\mathbf{v}_q\}_{q=1}^{N_d}$ denotes the standard basis of $\mathbb{R}^{N_d}$, and $\{p_1, p_2, \ldots, p_{N_s}\}$ are the finite difference nodes that lie within the region of influence of the $p \in K_\Omega$ node. Similarly, the nodal nonlocal pseudopotential matrix due to the J^{th} atom $\mathbf{V}_{nl,p}^J \in \mathbb{R}^{N_s \times N_s}$, and the nodal gradient $\tilde{\nabla}_{h,p} \equiv (\nabla_{xh,p} \in \mathbb{R}^{N_s \times N_s}, \nabla_{yh,p} \in \mathbb{R}^{N_s \times N_s}, \nabla_{zh,p} \in \mathbb{R}^{N_s \times N_s})$ are defined as

$$\mathbf{V}_{nl,p}^J = \mathbf{P}^T \mathbf{V}_{nl}^J \mathbf{P} , \tag{15}$$

$$\tilde{\nabla}_{h,p} = \mathbf{P}^T \tilde{\nabla}_h \mathbf{P} . \tag{16}$$

Analogously, $\mathbf{w}_p \in \mathbb{R}^{N_s \times 1}$ represents the restriction of the basis vector $\mathbf{v}_p$ to the region of influence of the $p \in K_\Omega$ node, i.e.,

$$\mathbf{w}_p = \mathbf{P}^T \mathbf{v}_p . \tag{17}$$

Chebyshev interpolation. In the Clenshaw-Curtis SQ method, functions of the nodal Hamiltonian are approximated in the Chebyshev polynomial basis. Specifically, the Chebyshev expansion of order n_{pl} for any function $f : [-1, 1] \to \mathbb{R}$ is of the form

$$f(\hat{\mathbf{H}}_p) = \sum_{j=0}^{n_{pl}} f_j T_j(\hat{\mathbf{H}}_p) , \tag{18}$$

where T_j denote the Chebyshev polynomials of degree j, and $\hat{\mathbf{H}}_p = (\mathbf{H}_p - \chi_p \mathbf{I})/\zeta_p$ is the scaled and shifted nodal Hamiltonian whose spectrum lies in the interval $[-1, 1]$. Here, $\mathbf{I} \in \mathbb{R}^{N_s \times N_s}$ denotes the identity matrix, $\chi_p = (\lambda_p^{max} + \lambda_p^{min})/2$ and $\zeta_p = (\lambda_p^{max} - \lambda_p^{min})/2$, with λ_p^{max} and λ_p^{min} denoting the maximum and minimum eigenvalues of $\mathbf{H}_p$, respectively. The expansion coefficients in Eqn. 18 can be evaluated using the relation

$$f_j = \frac{2}{\pi} \int_{-1}^{1} \frac{f(r) T_j(r)}{\sqrt{1 - r^2}} \, \mathrm{d}r , \quad j = 0, \ldots, n_{pl} , \tag{19}$$

where f_0 is further scaled by a factor of half. The column of $T_j(\hat{\mathbf{H}}_p)$ corresponding to the $p \in K_\Omega$ node, represented by $\mathbf{t}_p^j \in \mathbb{R}^{N_s \times 1}$, can be determined using the three term recurrence relation for Chebyshev polynomials:

$$\begin{aligned} \mathbf{t}_p^{j+1} &= 2\hat{\mathbf{H}}_p \mathbf{t}_p^j - \mathbf{t}_p^{j-1}\,, \\ \mathbf{t}_p^1 &= \hat{\mathbf{H}}_p \mathbf{w}_p\,,\ \mathbf{t}_p^0 = \mathbf{w}_p\,, \end{aligned} \tag{20}$$

with

$$\rho_p^j = \mathbf{w}_p^T \mathbf{t}_p^j \tag{21}$$

denoting the corresponding diagonal element.

3.2. Electron density

The electron density (Eqn. 2) needs to be evaluated in each iteration of the SCF method. In order to achieve this in $\mathcal{O}(N)$ fashion, we first utilize the exponential decay in the density matrix to express the electron density at the $p \in K_\Omega$ finite-difference node as

$$\rho_p = \frac{2}{h^3}\mathbf{v}_p^T g(\mathbf{H}, \mu, \sigma)\mathbf{v}_p \approx \frac{2}{h^3}\mathbf{w}_p^T g(\mathbf{H}_p, \mu, \sigma)\mathbf{w}_p = \frac{2}{h^3}\mathbf{w}_p^T g(\hat{\mathbf{H}}_p, \hat{\mu}_p, \hat{\sigma}_p)\mathbf{w}_p\,, \tag{22}$$

where $\hat{\sigma}_p = \sigma/\zeta_p$ denotes the scaled smearing, and $\hat{\mu}_p = (\mu - \chi_p)/\zeta_p$ denotes the scaled and shifted Fermi energy. Next, we approximate the Fermi-Dirac function in a Chebyshev polynomial basis to arrive at

$$\rho_p \approx \frac{2}{h^3}\mathbf{w}_p^T \left(\sum_{j=0}^{n_{pl}} c_p^j(\mu) T_j(\hat{\mathbf{H}}_p) \right) \mathbf{w}_p = \frac{2}{h^3} \sum_{j=0}^{n_{pl}} c_p^j(\mu)\rho_p^j\,, \tag{23}$$

where ρ_p^j are determined using Eqns. 20 and 21. The electron density at the $p \in K_\Omega$ node can therefore be expressed as

$$\rho_p = \frac{2}{h^3} \sum_{j=0}^{n_{pl}} c_p^j \rho_p^j\,, \tag{24}$$

where the expansion coefficients c_p^j correspond to the Fermi energy μ that results in the correct number of total electrons, i.e.,

$$2 \sum_{p \in K_\Omega} \sum_{j=0}^{n_{pl}} c_p^j(\mu)\rho_p^j = N_e\,. \tag{25}$$

During this process, the coefficients c_p^j are computed using Eqn. 19 by setting $f(r) = g(r, \hat{\mu}_p, \hat{\sigma}_p)$. The above expressions are applicable to both Γ-point and infinite-cell calculations, with the nodal quantities appropriately defined as described in Section 3.1.

We note the significant differences in the density calculation in Clenshaw-Curtis SQ and classical Chebyshev polynomial FOE. In the FOE approach, the complete density matrix is computed, whereas only its diagonal is computed in SQ. This can be seen in Eqn. 23, where the vectors $\mathbf{w}_p$ are moved inside the summation to form the scalars ρ_p^j. Indeed, such a procedure involves the calculation of the local vectors $\mathbf{t}_p^j$ using the recursive relation Eqn. 20. However, the truncated columns of the density matrix, which correspond to the local vectors $\sum_{j=0}^{n_{pl}} c_p^j \mathbf{t}_p^j$, are not computed in the SQ method. Furthermore, since the scalars ρ_p^j can be stored, the SQ approach allows for efficient determination of the Fermi energy μ, without recomputation

or storage of the Chebyshev matrices, as typically done in FOE. Finally, the key operations in SQ are local matrix-vector multiplications, compared to global matrix-matrix multiplications in FOE. The evaluation of the free energy in SQ proceeds along similar lines and does not involve the calculation of the density matrix, as further described below.

3.3. Free energy

The free energy (Eqn. 11) can be evaluated once the electronic ground-state is determined. Since the density matrix is not computed within the SQ method, the band structure energy and electronic entropy cannot be directly evaluated. In view of this, we develop expressions for the calculation of these quantities, as described below.

Band structure energy. Utilizing the same procedure and approximations as in the case of the electron density, the band structure energy takes the form

$$\begin{aligned} E_{band} &= 2\sum_{p\in K_\Omega} \mathbf{v}_p^T \left(\mathbf{H}^* g(\mathbf{H}^*,\mu,\sigma)\right)\mathbf{v}_p \approx 2\sum_{p\in K_\Omega} \mathbf{w}_p^T \left(\mathbf{H}_p^* g(\mathbf{H}_p^*,\mu,\sigma)\right)\mathbf{w}_p \\ &= 2\sum_{p\in K_\Omega} \mathbf{w}_p^T \left[(\chi_p + \zeta_p \hat{\mathbf{H}}_p^*) g(\hat{\mathbf{H}}_p^*,\hat{\mu}_p,\hat{\sigma}_p)\right]\mathbf{w}_p \\ &\approx 2\sum_{p\in K_\Omega} \mathbf{w}_p^T \left[\chi_p \sum_{j=0}^{n_{pl}} c_p^j T_j(\hat{\mathbf{H}}_p^*) + \zeta_p \sum_{j=0}^{n_{pl}} d_p^j T_j(\hat{\mathbf{H}}_p^*)\right]\mathbf{w}_p \\ &= 2\sum_{p\in K_\Omega}\sum_{j=0}^{n_{pl}} (\chi_p c_p^j + \zeta_p d_p^j)\rho_p^{j*}\,, \end{aligned} \tag{26}$$

where d_p^j are the coefficients of the Chebyshev expansion obtained by setting $f(r) = rg(r,\hat{\mu}_p,\hat{\sigma}_p)$ in Eqn. 19.

Electronic entropy. The electronic entropy can similarly be written as

$$\begin{aligned} S &= 2k_B \sum_{p\in K_\Omega} \mathbf{v}_p^T \left[g(\mathbf{H}^*,\mu,\sigma)\log g(\mathbf{H}^*,\mu,\sigma) + (\mathbf{I} - g(\mathbf{H}^*,\mu,\sigma))\log\left(\mathbf{I} - g(\mathbf{H}^*,\mu,\sigma)\right)\right]\mathbf{v}_p \\ &\approx 2k_B \sum_{p\in K_\Omega} \mathbf{w}_p^T \left[g(\hat{\mathbf{H}}_p^*,\hat{\mu}_p,\hat{\sigma}_p)\log g(\hat{\mathbf{H}}_p^*,\hat{\mu}_p,\hat{\sigma}_p) + \left(\mathbf{I} - g(\hat{\mathbf{H}}_p^*,\hat{\mu}_p,\hat{\sigma}_p)\right)\log\left(\mathbf{I} - g(\hat{\mathbf{H}}_p^*,\hat{\mu}_p,\hat{\sigma}_p)\right)\right]\mathbf{w}_p \\ &\approx 2k_B \sum_{p\in K_\Omega} \mathbf{w}_p^T \left[\sum_{j=0}^{n_{pl}} e_p^j T_j(\hat{\mathbf{H}}_p^*)\right]\mathbf{w}_p \\ &= 2k_B \sum_{p\in K_\Omega}\sum_{j=0}^{n_{pl}} e_p^j \rho_p^{j*}\,, \end{aligned} \tag{27}$$

where e_p^j are calculated using Eqn. 19 by setting

$$f(r) = g(r,\hat{\mu}_p,\hat{\sigma}_p)\log g(r,\hat{\mu}_p,\hat{\sigma}_p) + (1 - g(r,\hat{\mu}_p,\hat{\sigma}_p))\log(1 - g(r,\hat{\mu}_p,\hat{\sigma}_p)).$$

Free Energy. Using the band structure energy in Eqn. 26, and the electronic entropy in Eqn. 27, the free energy in Eqn. 11 can be written as

$$\begin{aligned}\mathcal{F}_0(\mathbf{R}) &= h^3 \sum_{p\in K_\Omega} \left(\frac{2}{h^3} \sum_{j=0}^{n_{pl}} (\chi_p c_p^j + \zeta_p d_p^j)\rho_p^{j*} + \varepsilon_{xc}(\rho_p^*)\rho_p^* + \frac{1}{2}(b_p - \rho_p^*)\phi_p^* - V_{xc}(\rho_p^*)\rho_p^* \right. \\ &\left. + \frac{1}{2}(\tilde{b}_p + b_p)V_{c,p} - \frac{1}{2}\sum_J \tilde{b}_{J,p}\tilde{V}_{J,p} + \frac{2\sigma}{h^3}\sum_{j=0}^{n_{pl}} e_p^j \rho_p^{j*} \right), \end{aligned} \tag{28}$$

where the integrals have been approximated using the trapezoidal rule (Eqn. 38). The subscript p is used to denote the value of the corresponding quantity at that finite-difference node. As before, the summation index J runs over all the atoms in Ω and their periodic replicas. The free energy expression in Eqn. 28 is applicable to both Γ-point and infinite cell calculations, with the nodal quantities defined appropriately as described in Section 3.1.

3.4. Atomic forces

The atomic forces (Eqn. 12)—required for structural relaxations and molecular dynamics—need to be calculated once the electronic ground-state is determined. They consist of local and nonlocal components, whose expressions we present below.

Local component. The local component of the atomic force takes the form

$$\begin{aligned}\mathbf{f}_I^l &= h^3 \sum_{I'} \sum_{p\in K_\Omega} \left(\tilde{\nabla}_h b_{I'}\big|_p (\phi_p^* - V_{I',p}) + \frac{1}{2}\tilde{\nabla}_h \tilde{b}_{I'}\big|_p \left(V_{c,p} - \tilde{V}_{I',p}\right) + \frac{1}{2}\tilde{\nabla}_h b_{I'}\big|_p \left(V_{c,p} + V_{I',p}\right) \right. \\ &\left. + \frac{1}{2}\tilde{\nabla}_h V_{c,I'}\big|_p \left(\tilde{b}_p + b_p\right) + \frac{1}{2} b_{I',p}\tilde{\nabla}_h V_{I'}\big|_p - \frac{1}{2}\tilde{b}_{I',p}\tilde{\nabla}_h \tilde{V}_{I'}\big|_p \right), \end{aligned} \tag{29}$$

where the integrals have been approximated using the trapezoidal rule (Eqn. 38). Again, the summation index I' runs over the I^{th} atom and all its periodic images.

Nonlocal component. The nonlocal component of the force—as formulated in Appendix B—for a Γ-point calculation can be written as

$$\mathbf{f}_I^{nl} = 4 \sum_{p\in K_\Omega} \mathbf{v}_p^T \left(\mathbf{V}_{nl}^I \tilde{\nabla}_h g(\mathbf{H}^*, \mu, \sigma) \right) \mathbf{v}_p \,. \tag{30}$$

After approximating the above expression in terms of the local density matrix and expanding in Chebyshev polynomials, we arrive at

$$\mathbf{f}_I^{nl} \approx 4 \sum_{p\in K_\Omega} \mathbf{w}_p^T \left(\mathbf{V}_{nl,p}^I \tilde{\nabla}_{h,p} g(\hat{\mathbf{H}}_p^*, \hat{\mu}_p, \hat{\sigma}_p) \right) \mathbf{w}_p \approx 4 \sum_{p\in K_\Omega} \sum_{j=0}^{n_{pl}} c_p^j \mathbf{w}_p^T \mathbf{V}_{nl,p}^I \tilde{\nabla}_{h,p} \mathbf{t}_p^{j*} \,. \tag{31}$$

An alternative approach for determining the nonlocal component of the force involves individually evaluating the required diagonal- and off-diagonal components of the local density matrix using SQ. However, such a strategy is computationally expensive due to the large number of density matrix components required. This is overcome in Clenshaw-Curtis SQ using the observation that required diagonal- and off-diagonal density matrix components can be written in terms of $\mathbf{t}_p^{j*}$, which are available during the recursive iteration in Eqn. 20. However, in Gauss SQ, the required components of the density matrix need to be individually computed, which makes calculation of the atomic forces considerably more expensive.

Total force. Using the local component of the force in Eqn. 29, and the nonlocal component of the force in Eqn. 31, the atomic force in Eqn. 12 can be written as

$$\begin{aligned}\mathbf{f}_I &= h^3 \sum_{I'} \sum_{p\in K_\Omega} \Bigg(\tilde{\nabla}_h b_{I'}\big|_p (\phi^*_p - V_{I',p}) + \frac{1}{2}\tilde{\nabla}_h \tilde{b}_{I'}\big|_p \left(V_{c,p} - \tilde{V}_{I',p}\right) + \frac{1}{2}\tilde{\nabla}_h b_{I'}\big|_p \left(V_{c,p} + V_{I',p}\right) \\ &+ \frac{1}{2}\tilde{\nabla}_h V_{c,I'}\big|_p \left(\tilde{b}_p + b_p\right) + \frac{1}{2} b_{I',p}\tilde{\nabla}_h V_{I'}\big|_p - \frac{1}{2}\tilde{b}_{I',p}\tilde{\nabla}_h \tilde{V}_{I'}\big|_p \Bigg) \\ &- 4 \sum_{p\in K_\Omega} \sum_{j=0}^{n_{pl}} c^j_p \mathbf{w}_p^T \mathbf{V}^I_{nl,p} \tilde{\nabla}_{h,p} \mathbf{t}^{j*}_p \,. \end{aligned} \tag{32}$$

For an infinite-cell calculation, while the local component of the force remains the same, the nonlocal component differs because of the different boundary conditions imposed on the nonlocal pseudopotential in Γ-point and infinite-cell calculations, as can be seen from Eqns. 39 and 40 (and the discussion below them). Adopting the same procedure as for the nonlocal Γ-point force, we arrive at the following expression for total atomic force in infinite-cell calculations:

$$\begin{aligned}\mathbf{f}^\infty_I &= h^3 \sum_{I'} \sum_{p\in K_\Omega} \Bigg(\tilde{\nabla}_h b_{I'}\big|_p (\phi^*_p - V_{I',p}) + \frac{1}{2}\tilde{\nabla}_h \tilde{b}_{I'}\big|_p \left(V_{c,p} - \tilde{V}_{I',p}\right) + \frac{1}{2}\tilde{\nabla}_h b_{I'}\big|_p \left(V_{c,p} + V_{I',p}\right) \\ &+ \frac{1}{2}\tilde{\nabla}_h V_{c,I'}\big|_p \left(\tilde{b}_p + b_p\right) + \frac{1}{2} b_{I',p}\tilde{\nabla}_h V_{I'}\big|_p - \frac{1}{2}\tilde{b}_{I',p}\tilde{\nabla}_h \tilde{V}_{I'}\big|_p - \frac{4}{h^3}\sum_{j=0}^{n_{pl}} c^j_p \mathbf{w}_p^T \mathbf{V}^{I'}_{nl,p} \tilde{\nabla}_{h,p} \mathbf{t}^{j*}_p \Bigg) \end{aligned} \tag{33}$$

In deriving the nonlocal component of the force in the above equation, since $\mathbf{t}^{j*}_p$ is not available for $p \notin K_\Omega$, it has been periodically mapped back to the corresponding $\mathbf{t}^{j*}_p$ for $p \in K_\Omega$.

4. Numerical Implementation

In this section, we describe a high-order finite-difference implementation of the formulation presented in the previous section. We consider cubical domains Ω and Ω', whose edge lengths are denoted using the common notation L. We employ a uniform finite-difference grid with spacing h such that $L = n_d h$, where n_d is the number of grid points in each direction. We index the grid points by (i, j, k), where $i, j, k = 1, 2, \ldots, n_d$. We approximate the Laplacian of a function $f(\mathbf{x})$ at the grid point (i, j, k) using high-order finite-differences [43]

$$\nabla^2_h f\big|^{(i,j,k)} \approx \sum_{q=0}^{n_o} w_q \Big(f^{(i+q,j,k)} + f^{(i-q,j,k)} + f^{(i,j+q,k)} + f^{(i,j-q,k)} + f^{(i,j,k+q)} + f^{(i,j,k-q)} \Big) \,, \tag{34}$$

where $f^{(i,j,k)}$ represents the value of the function $f(\mathbf{x})$ at the grid point (i, j, k). The weights are of the form [44, 45, 46]

$$\begin{aligned} w_0 &= -\frac{1}{h^2}\sum_{r=1}^{n_o} \frac{1}{r^2} \,, \\ w_q &= \frac{2(-1)^{q+1}}{h^2 q^2} \frac{(n_o!)^2}{(n_o - q)!(n_o + q)!} \,, \quad q = 1, 2, \ldots, n_o. \end{aligned} \tag{35}$$

Similarly, we approximate the gradient $\tilde{\nabla}_h \equiv (\nabla_{xh}, \nabla_{yh}, \nabla_{zh})$ as

$$\begin{aligned}
\nabla_{xh} f\big|^{(i,j,k)} &= \sum_{q=1}^{n_o} \tilde{w}_q \left(f^{(i+q,j,k)} - f^{(i-q,j,k)} \right) , \\
\nabla_{yh} f\big|^{(i,j,k)} &= \sum_{q=1}^{n_o} \tilde{w}_q \left(f^{(i,j+q,k)} - f^{(i,j-q,k)} \right) , \\
\nabla_{zh} f\big|^{(i,j,k)} &= \sum_{q=1}^{n_o} \tilde{w}_q \left(f^{(i,j,k+q)} - f^{(i,j,k-q)} \right) ,
\end{aligned} \tag{36}$$

where the weights [44, 45, 46]

$$\tilde{w}_q = \frac{(-1)^{q+1}}{hq} \frac{(n_o!)^2}{(n_o - q)!(n_o + q)!} , \; q = 1, 2, \ldots, n_o. \tag{37}$$

These finite-difference expressions for the Laplacian and gradient represent $2n_o$-order accurate approximations, i.e., error $\mathcal{O}(h^{2n_o})$. While performing spatial integrations, we assume that the function $f(\mathbf{x})$ is constant in a cube of side h around each grid point. For example, in a Γ-point calculation

$$\int_\Omega f(\mathbf{x}) \, \mathrm{d}\mathbf{x} \approx h^3 \sum_{i,j,k}^{n_d} f^{(i,j,k)}. \tag{38}$$

For periodic integrands, this is equivalent to a trapezoidal rule. Using this rule, we approximate the nonlocal pseudopotential operator in Γ-point calculations as

$$\mathcal{V}_{nl} f\big|^{(i,j,k)} = \sum_I \mathcal{V}_{nl}^I f\big|^{(i,j,k)} \approx h^3 \sum_I \sum_{lm} \sum_{p,q,r}^{n_d} \gamma_l^I \chi_{lm}^{I(i,j,k)} \chi_{lm}^{I(p,q,r)} f^{(p,q,r)} , \tag{39}$$

where the summation index I runs over all atoms in Ω. Analogously, for infinite-cell calculations

$$\mathcal{V}_{nl}^\infty f\big|^{(i,j,k)} = \sum_J \mathcal{V}_{nl}^J f\big|^{(i,j,k)} \approx h^3 \sum_J \sum_{lm} \sum_{p,q,r}^{n_d} \gamma_l^J \chi_{lm}^{J(i,j,k)} \chi_{lm}^{J(p,q,r)} f^{(p,q,r)} . \tag{40}$$

where the summation index J runs over all atoms in Ω as well as their periodic images. Since the projectors of each atom are localized in real-space, the nonlocal pseudopotential matrix can be created in $\mathcal{O}(N)$ fashion. We enforce periodic boundary conditions on Ω by employing the following strategy. In the finite-difference representations of the Laplacian, gradient, and the nonlocal pseudopotential as presented in Eqns. 34, 36 and 39 respectively, we map any index that does not correspond to a node in the finite-difference grid in Ω to its periodic image within Ω. Similarly, we enforce zero Dirichlet boundary conditions on Ω' by setting $f^{(i,j,k)} = 0$ for any index that does not correspond to a node in the finite-difference grid.

We generate the initial electron density for the Self-Consistent Field (SCF) iteration by superposing isolated-atom electron densities. We do so by visiting only atoms whose isolated-atom electron densities have nonzero overlap with Ω. Similarly, we calculate the charge density of the nuclei using the relations

$$b^{(i,j,k)} = \sum_J b_J^{(i,j,k)} , \quad b_J^{(i,j,k)} = -\frac{1}{4\pi} \nabla^2 V_J\big|^{(i,j,k)} , \tag{41}$$

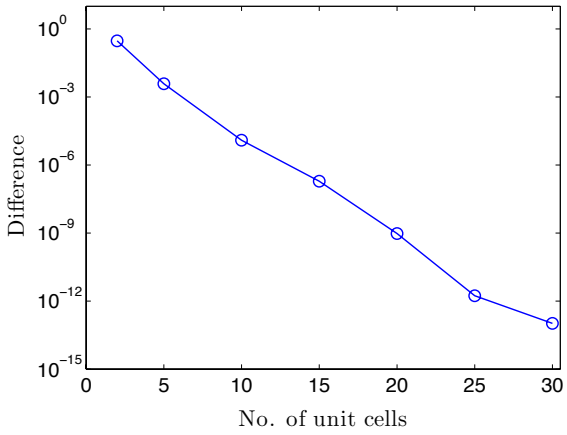

Figure 2: Convergence of the Γ-point energy to the infinite-cell limit for a 1D model problem. The energy corresponding to a 40 unit-cell system has been used as reference.

where the summation reduces in practice to all atoms whose charge density has nonzero overlap with Ω. The localized nature of the above operations ensures that the evaluation of $b^{(i,j,k)}$ scales as $\mathcal{O}(N)$. In every iteration of the SCF method—accelerated using Anderson extrapolation [47]—we solve the Poisson equation (Eqn. 10) subject to periodic boundary conditions on Ω using the Minimum Residual (MINRES) method [48]. Since the solution so obtained is unique only up to an arbitrary constant, we enforce the condition $\phi^{(1,1,1)} = 0$ for definiteness. In every subsequent Poisson equation encountered, we use the previous solution as starting guess. We evaluate the electron density, energy, and atomic forces using the expressions developed in Section 3. Proceeding in this way, the overall computational complexity is $\mathcal{O}(N)$ since all calculations are local and independent of system size. We note that sophisticated preconditioners such as multigrid [49] must be employed for the Poisson equation in order to achieve $\mathcal{O}(N)$ scaling in practice. However, since the Poisson solve constitutes a small fraction of the total computation in our current serial implementation, such preconditioning schemes have not been employed in the present work.

5. Results and Discussion

In this section, we verify the convergence of the Clenshaw-Curtis Spectral Quadrature (SQ) method for canonical insulating and metallic systems. Specifically, we demonstrate convergence with respect to quadrature order and truncation radius to the diagonalization result. We also show convergence with respect to mesh size to established $\mathcal{O}(N^3)$ scaling planewave results. To allow rigorous assessment of convergence, we first consider a model one-dimensional problem in Section 5.1. We then consider full, three-dimensional Kohn-Sham calculations in Section 5.2. Finally, we study the efficiency of SQ for performing high temperature calculations in Section 5.3, and its suitability for scalable high performance computing in Section 5.4.

5.1. Model problem

We begin with a one-dimensional model problem wherein atoms interact with the effective potential [50]

$$V_{\mathit{eff}}(x, \mathbf{R}) = -\sum_{J} \frac{\alpha}{\sqrt{2\pi\beta^2}} \exp\left(-\frac{(x - R_J)^2}{2\beta^2}\right). \tag{42}$$

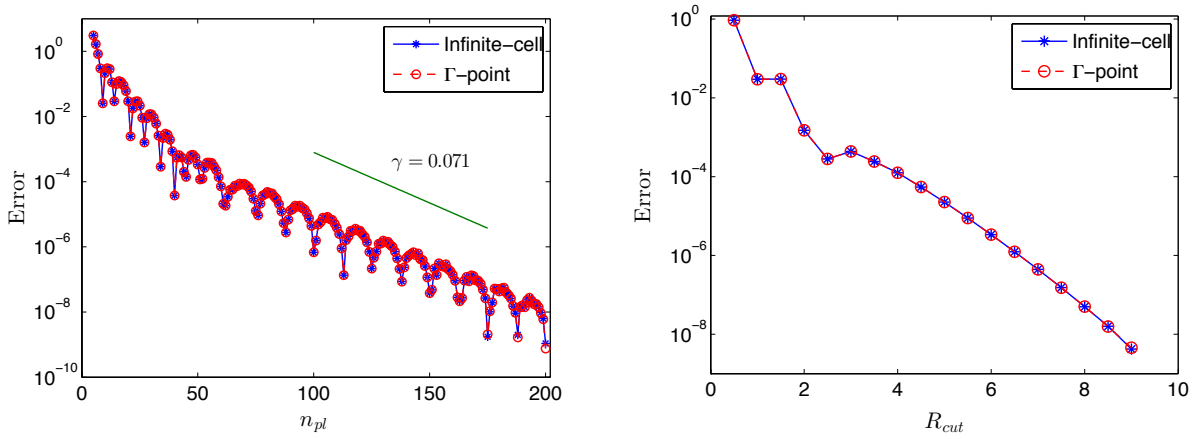

(a) Convergence with n_{pl}

(b) Convergence with R_{cut}

Figure 3: Convergence of energy with respect to quadrature order n_{pl} and truncation radius R_{cut} to the diagonalization result for a 1D model problem. 2-atom and 25-atom unit cells have been employed for the infinite-cell and Γ-point calculations, respectively. The theoretically predicted convergence rate [25] is denoted by γ.

We choose the parameters $(\alpha, \beta) = (10, 0.6)$, and consider an infinite chain of atoms with unit lattice constant. In addition, we employ a twelfth order finite-difference discretization with a mesh-size of $h = 0.1$, and a smearing of $\sigma = 1$. In Fig. 2, we show the convergence of the Γ-point energy (obtained via diagonalization) to the infinite-cell result as the number of unit cells (containing one atom each) in Ω is increased. We see that the energy has converged to within $\sim 10^{-12}$ of the infinite-unit-cell limit for Ω containing 25 unit cells. In order to validate the SQ method, we therefore choose 2-atom and 25-atom cells for the infinite-cell and Γ-point calculations, respectively. The converged energies for each case should then differ by no more than $\sim 10^{-12}$.

The two parameters introduced by the Clenshaw-Curtis SQ method are the order of the quadrature n_{pl} and the truncation radius R_{cut}. In Fig. 3, we show the convergence with respect to these two parameters for both Γ-point and infinite-cell calculations. Specifically, we plot the error in energy—defined with respect to the result obtained by diagonalization—versus n_{pl} and R_{cut} in Figs. 3a and 3b, respectively. Since the cell Ω in the Γ-point calculations has been chosen sufficiently large to reduce finite-size effects to $\sim 10^{-12}$, the Γ-point and infinite-cell results should be essentially indistinguishable, as we see in Fig. 3. We observe that SQ demonstrates exponential convergence with respect to n_{pl}, with the obtained rate in excellent agreement with theoretical predictions [25]. Moreover, there is exponential convergence with respect to R_{cut}, again in agreement with theory [37].

Apart from the Clenshaw-Curtis SQ method developed in the present work, the other notable variant of SQ is based on Gauss quadrature [25]. For the 1D model problem, in Figs. 4a and 4b, we compare the convergence of the two approaches with respect to n_{pl} and R_{cut}, respectively. These results correspond to Γ-point (convergence with n_{pl}) and infinite-cell (convergence with R_{cut}) calculations for 25-atom and 2-atom unit cells, respectively. We observe that the asymptotic convergence rate of Gauss SQ is twice that of Clenshaw-Curtis SQ, and both are in good agreement with theoretical predictions [25]. Notably, the initial convergence rate of Clenshaw-Curtis SQ is twice its asymptotic value, a phenomenon which has been discussed in detail elsewhere [51]. The convergence of both methods with respect to R_{cut} is identical, as dictated by the decay of the density matrix.

In Clenshaw-Curtis SQ, the key computations occurring for every finite-difference node are the n_{pl} local

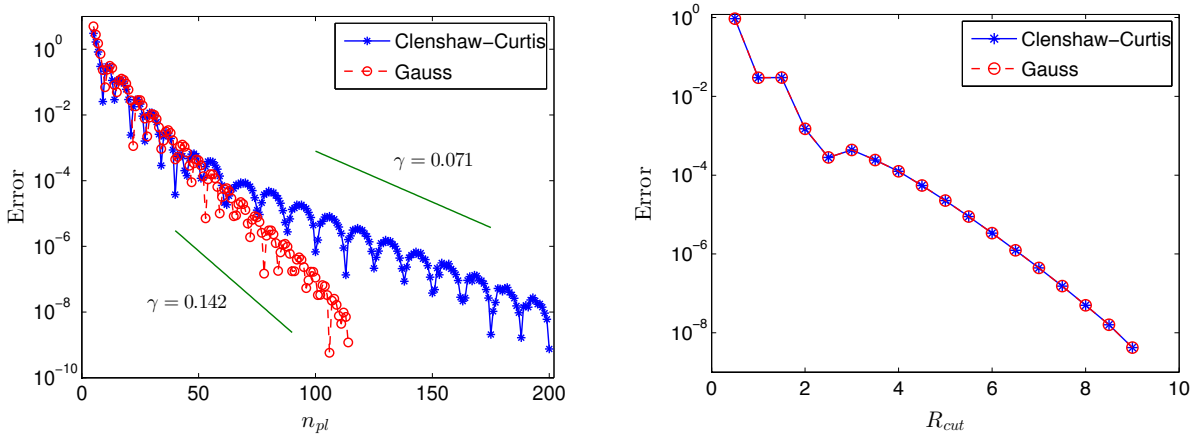

(a) Convergence with n_{pl}

(b) Convergence with R_{cut}

Figure 4: Comparison of the convergence of the Clenshaw-Curtis and Gauss SQ methods to the diagonalization result for a 1D model problem. 2-atom and 25-atom unit cells have been employed for the infinite-cell (convergence with R_{cut}) and Γ-point (convergence with n_{pl}) calculations, respectively. The theoretically predicted convergence rate [25] is denoted by γ.

matrix-vector multiplications, and evaluation of the n_{pl} Chebyshev expansion coefficients. In practical DFT calculations, the relatively large nodal Hamiltonians result in the matrix-vector products being the dominant computational cost. Similarly, the dominant cost in Gauss SQ corresponds to the n_{pl} local matrix-vector multiplications during the Lanczos iteration, with the tridiagonal matrix orthogonalization constituting a relatively small fraction of the total expense. It is evident from Fig. 4a that the quadrature order required by Gauss SQ is typically smaller than for Clenshaw-Curtis SQ. However, since both approaches display similar convergence behavior in the initial stages, the quadrature orders required for achieving chemical accuracies do not differ significantly. In this work, we have preferred the Clenshaw-Curtis variant of SQ since the nonlocal component of the atomic forces can be evaluated straightforwardly and efficiently (Section 3.4), whereas the path to such is unclear for Gauss SQ. In addition, the evaluation of the Chebyshev coefficients in Clenshaw-Curtis SQ scales as $\mathcal{O}(n_{pl} \log n_{pl})$ [52], whereas orthogonalization of the tridiagonal matrix in Gauss SQ scales as $\mathcal{O}(n_{pl}^2)$ [53].

5.2. Kohn-Sham calculations

We consider two systems for the Kohn-Sham calculations: (i) lithium hydride, a prototypical insulator, and (ii) aluminum, a prototypical metal. In all simulations, we use norm-conserving Troullier-Martins pseudopotentials [54], and the Perdew-Wang parametrization [55] of the correlation energy calculated by Ceperley-Alder [56]. Additionally, we utilize a smearing of 0.5 eV and 4 eV for the Γ-point and infinite-cell calculations, respectively. Finally, we employ a twelfth order accurate finite-difference discretization, unless otherwise specified.

5.2.1. Lithium hydride

We consider an 8-atom unit cell of lithium hydride at the equilibrium lattice constant of 7.37 Bohr. We displace the lithium atom at the corner of the unit cell, which corresponds to the origin of the chosen coordinate system, to $[0.57\ 0.43\ 0.37]$ Bohr. For lithium's nonlocal pseudopotential, we designate the s channel as local, and utilize cutoff radii of 2.43 Bohr for both the s and p channels. For hydrogen's pseudopotential, we use a cutoff radius of 1.4 Bohr. We perform both Γ-point and infinite-cell calculations

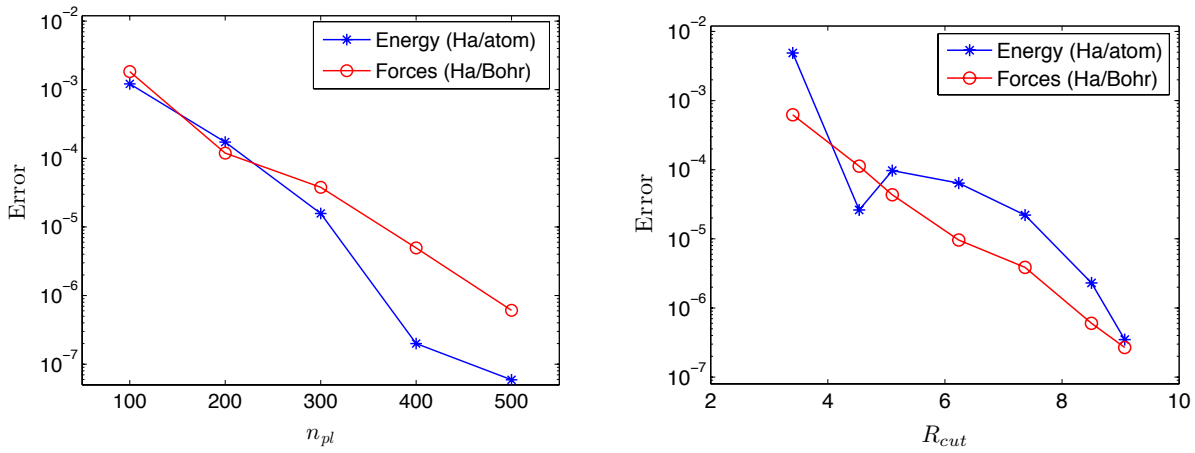

(a) Γ-point calculation

(b) Infinite-cell calculation

Figure 5: Convergence of energy and forces with respect to quadrature order n_{pl} and truncation radius R_{cut} to the diagonalization result for lithium hydride. The error in energy denotes the magnitude of the difference, and error in forces represents the maximum difference in any component.

with $h = 0.57$ Bohr, and present the results so obtained in Fig. 5. Specifically, we plot the convergence of SQ energy and forces with respect to quadrature order n_{pl} and truncation radius R_{cut} for Γ-point and infinite-cell calculations in Figs. 5a and 5b, respectively. The errors are defined relative to the results obtained by diagonalization. As in the case of the one-dimensional model problem, we obtain exponential convergence with respect to both parameters. These results indicate that the theoretical predictions made in the linear setting [25, 37] are also applicable to the nonlinear Kohn-Sham problem. We note that neither energies nor forces are variational with respect to R_{cut}, and so errors can in general be positive, negative, or zero. This can be seen, for example, in the non-monotonic convergence of the energy error in Fig. 5b.

Next, we verify the accuracy of SQ by comparing the calculated energies and forces to those computed by the ABINIT planewave code [57]. In ABINIT, we employ a planewave cutoff of 50 Ha, and a $6 \times 6 \times 6$ Monkhorst-Pack grid for Brillouin zone integration. These parameters result in energies and forces converged to within 10^{-6} Ha/atom and 10^{-6} Ha/Bohr, respectively. In SQ, wherever it is not possible to utilize twelfth order finite-differences, we employ the largest order feasible. Additionally, we utilize $\{n_{pl}, R_{cut}\} = \{550, 3.69\,\text{Bohr}\}$ and $\{n_{pl}, R_{cut}\} = \{160, 8.50\,\text{Bohr}\}$ for the Γ-point and infinite-cell calculations, respectively. These values are sufficient to put the associated errors well below the mesh errors of interest. We note that a larger value of n_{pl} is required for the Γ-point calculation because of the lower value of smearing/temperature. As shown in Fig. 6, both energies and forces in SQ converge rapidly and systematically, with chemical accuracy easily obtained. Notably, we see that energies and forces converge at comparable rates, without need of additional measures such as double-grid [58] or high-order integration [24] techniques. Hence, accurate forces are easily obtained, as required for structural relaxation and molecular dynamics simulations.

5.2.2. Aluminum

We now consider a 4-atom face-centered cubic (FCC) unit cell of aluminum at the equilibrium lattice constant of 7.78 Bohr. We move the atom located at [3.89 3.89 0.00] Bohr to [3.74 3.49 0.37] Bohr, with the corner atom again coinciding with the origin. We utilize a nonlocal pseudopotential having cutoff radii of 2.58 Bohr for both the s and p channels, with the p channel chosen as local. In Fig. 7, we show

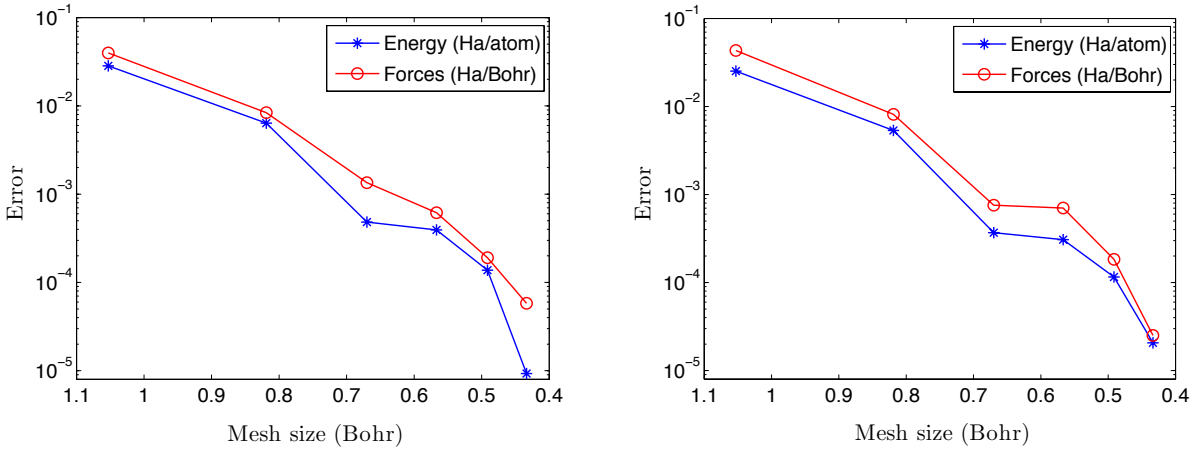

(a) Γ-point calculation (b) Infinite-cell calculation

Figure 6: Convergence of energy and forces with respect to mesh size to reference planewave result for lithium hydride. The error in energy denotes the magnitude of the difference, and error in forces represents the maximum difference in any component.

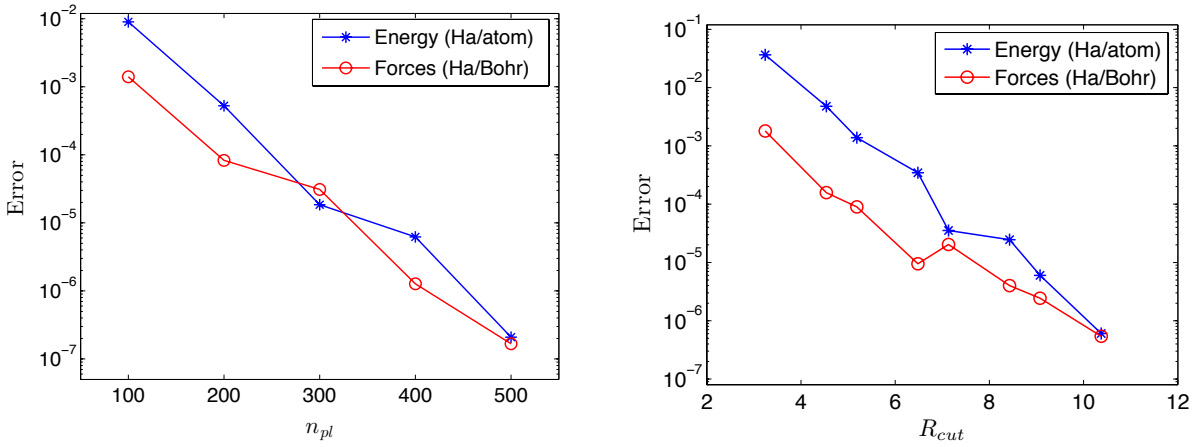

(a) Γ-point calculation (b) Infinite-cell calculation

Figure 7: Convergence of energy and forces with respect to quadrature order n_{pl} and truncation radius R_{cut} to the diagonalization result for aluminum. The error in energy denotes the magnitude of the difference, and error in forces represents the maximum difference in any component.

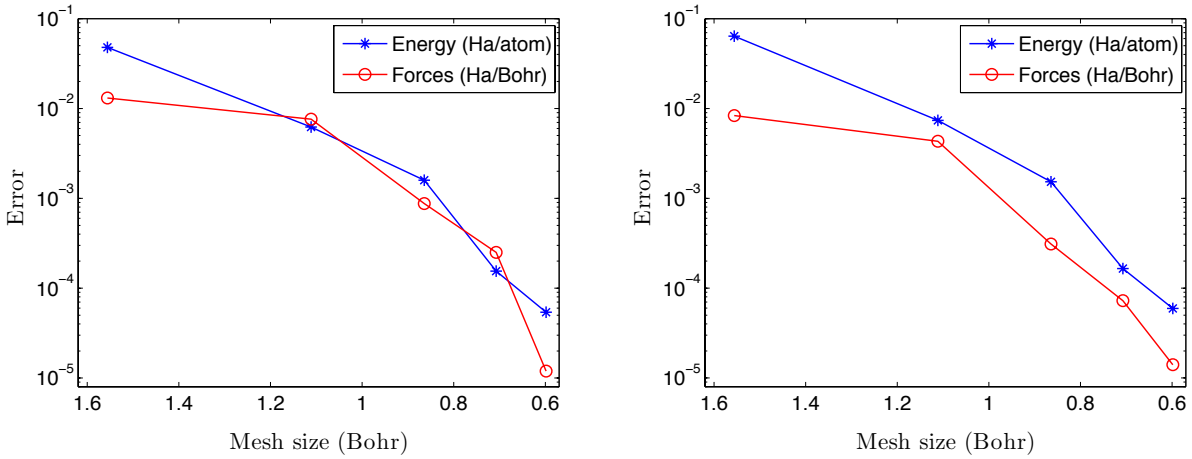

(a) Γ-point calculation

(b) Infinite-cell calculation

Figure 8: Convergence of energy and forces with respect to mesh size to reference planewave result for aluminum. The error in energy denotes the magnitude of the difference, and error in forces represents the maximum difference in any component.

the convergence of energy and forces with respect to quadrature order n_{pl} for Γ-point calculations, and truncation radius R_{cut} for infinite-cell calculations. We choose $h = 0.65$ Bohr for the calculations and define all errors with respect to diagonalization. For this prototypical metallic system, we obtain exponential convergence with respect to both parameters, just as for the insulating lithium hydride system.

Finally, we compare the results obtained by SQ and ABINIT for the aforedescribed aluminum system. In ABINIT, we utilize a planewave cutoff of 30 Ha, and a $6 \times 6 \times 6$ Monkhorst-Pack grid for Brillouin zone integration. The energies and forces so computed are converged to within 10^{-6} Ha/atom and 10^{-6} Ha/Bohr, respectively. In SQ, whenever n_d is too small to utilize twelfth order finite-differences, we again employ the largest order possible. Additionally, we utilize $\{n_{pl}, R_{cut}\} = \{600, 3.89\,\text{Bohr}\}$ and $\{n_{pl}, R_{cut}\} = \{120, 10.00\,\text{Bohr}\}$ for the Γ-point and infinite-cell calculations, respectively. It is clear from the results presented in Fig. 8 that similar to the case of lithium hydride, both energies and forces converge rapidly, and at similar rates. Overall, we see that SQ is able to obtain chemical accuracy in both energies and forces, straightforwardly and systematically, in both insulating and metallic systems.

5.3. High temperature calculations

The computational cost of conventional diagonalization-based DFT calculations grows rapidly with increasing temperature due to a larger number of previously unoccupied states becoming partially occupied. Since most diagonalization algorithms scale quadratically with the number of states to be computed, high temperature calculations can quickly become intractable. However, in the Clenshaw-Curtis SQ method, the overall cost *decreases* with increasing temperature. This is due to the enhanced decay of the density matrix, which translates to smaller values of the truncation radius R_{cut}. Furthermore, a lower-order quadrature rule suffices due to the increased smoothness of the Fermi-Dirac function, resulting in additional savings. In order to quantify this reduction in quadrature order, we consider the Γ-point calculation for the aluminum system described in Section 5.2.2 at different temperatures, and determine the order of quadrature required to attain convergence of ~ 0.0001 Ha/atom in the energy and ~ 0.0001 Ha/Bohr in atomic forces. We present the results so obtained in Fig. 9, along with theoretically predicted convergence rates γ [25]. We observe that there is indeed a rapid decrease in the order of quadrature, and thus computational cost, re-

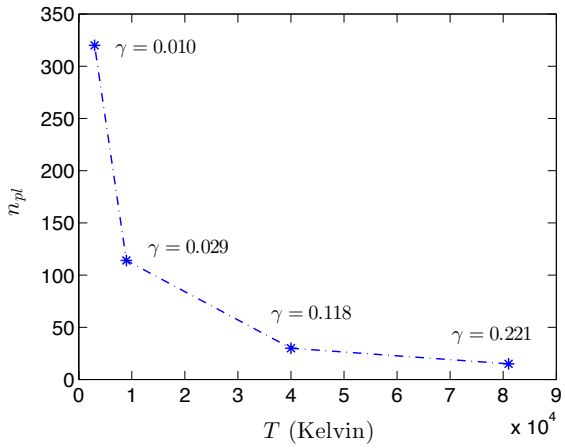

Figure 9: Dependence of quadrature order n_{pl} on temperature T for errors of ∼0.0001 Ha/atom in energy and ∼0.0001 Ha/Bohr in forces. The theoretically predicted convergence rate [25] is denoted by γ.

quired to obtain the specified accuracies as temperature increases. Moreover, the quadrature order required is consistent with the predicted convergence rate γ [25], which increases with temperature.

Since the required order of quadrature in SQ varies inversely with the temperature for a given spectral width [25], it can be inferred from Fig. 9 that quadrature orders of a few thousand are required for calculations near room temperature. Therefore, the SQ approach possesses a relatively large prefactor for such temperatures and/or Hamiltonians with large spectral width. However, the particular suitability of SQ for large-scale parallel computation, as discussed below, stands to mitigate this. Therefore, it may be expected that calculations at room temperature will be feasible using Clenshaw-Curtis SQ when sufficient processors are available. One helpful degree of freedom to exploit in practice is the use of larger occupation smearing than $\sigma = 0.001$ Ha ($T \sim 315$ K) as an approximation. The typical practice in metallic calculations of employing a smearing of $\sigma \sim 0.01$ Ha ($T \sim 3150$ K), for example, could yield substantial efficiency gains, while retaining energies and forces to high accuracy relative to $\sigma = 0.001$ Ha values.

5.4. Large-scale parallel implementation

Conventional $\mathcal{O}(N^3)$ scaling diagonalization-based electronic structure methods involve the computation of large numbers of orthonormal eigenvectors, which requires communication between each processor holding all or a part of an eigenvector and every other processor holding all or a part of other eigenvectors. This extensive communication severely limits parallel scalability. $\mathcal{O}(N)$ electronic structure methods compute required densities, energies, and forces, proceeding directly from Hamiltonian to required outputs without diagonalization. The key computational workload in standard $\mathcal{O}(N)$ electronic structure methods such as Fermi operator expansion (FOE) [28, 29] instead comes in the form of repeated large sparse matrix-matrix multiplies involving the Hamiltonian. However, with each multiply, the sparsity pattern changes, necessitating truncation to retain only desired nonzeros. Moreover, nonlocal communications and indirect addressing are required to map nonzeros of corresponding rows and columns to one another, making such operations difficult to parallelize at large scale.

Being integral based, however, the SQ electronic structure method admits a natural decomposition in real-space, eliminating the need for large sparse matrix-matrix operations entirely. To exploit this, we have represented the electronic densities and potentials on a uniform finite-difference grid in real-space. Moreover, we have exploited the locality of the density matrix to replace large global sparse matrix-matrix

operations by small local sparse matrix-vector operations, with all calculations strictly confined to localization regions around each grid point. In so doing, the key computational operations are reduced to local finite-difference stencil operations, global vector sums, and dot products. Storage and memory access can be minimized by forming local matrices on the fly, simultaneously at each grid point, and can be reduced further still by computing only the action of matrices on required vectors, rather than computing the matrices themselves. These latter possibilities arise naturally in the SQ formulation, allowing flops to be traded for decreased storage, access, and/or communication, as best suits the architecture at hand. By reducing all key computational kernels to local stencil and vector operations, the SQ method is well suited to large-scale parallel implementation.

6. Concluding Remarks

We have presented the Clenshaw-Curtis Spectral Quadrature (SQ) method for performing real-space $\mathcal{O}(N)$ Density Functional Theory (DFT) calculations. In this approach, all quantities of interest are expressed as bilinear forms, or sums over bilinear forms, which are then approximated by spatially localized Clenshaw-Curtis quadrature rules. In conjunction with the local reformulation of the electrostatics, the proposed approach enables the $\mathcal{O}(N)$ evaluation of the electronic density, energy, and atomic forces. In addition, the method permits infinite-cell calculations without recourse to Brillouin zone integration or large supercells. We have employed a high-order finite difference representation in order to exploit the locality of electronic interactions in real-space, enable systematic convergence, and facilitate large-scale parallel implementation. In this representation, we have developed expressions for the electronic density, total energy, and atomic forces which can be evaluated in $\mathcal{O}(N)$ operations.

The SQ energies and forces were shown to converge systematically with respect to quadrature order and truncation radius to the exact diagonalization result, for 1D model as well as full 3D Kohn-Sham calculations of insulating and metallic systems. Moreover, convergence to established $\mathcal{O}(N^3)$ scaling planewave results was obtained with increasing mesh. In both cases, chemical accuracy was readily attained. The efficiency of the approach for high temperature calculations was also shown, demonstrating decreasing cost with increasing temperature. Finally, the particular suitability of the SQ method for large-scale parallel computation was considered, reducing as it does all key computational kernels to local stencil and vector operations.

Having now completed and verified the prototype MATLAB implementation, current work focuses on the development of a massively parallel implementation for quantum molecular dynamics simulations of complex insulating and metallic systems.

7. Acknowledgements

This work was performed, in part, under the auspices of the U.S. Department of Energy by Lawrence Livermore National Laboratory under Contract DE-AC52-07-NA27344 and the Exascale Co-design Center for Materials in Extreme Environments supported by Office of Science Advanced Scientific Computing Research Program. The authors gratefully acknowledge the valuable comments and suggestions of the anonymous referee.

A. Electrostatic correction for overlapping nuclear densities

Large-scale electronic structure calculations typically employ the pseudopotential approximation. Even though this is the case, the repulsive energy is calculated with the nuclei treated as point charges. This distinction is not made by the formulation of electrostatics employed in this work, resulting in disagreement

with conventional methods if the nuclear charge densities overlap. The correction to the repulsive energy which restores agreement can be expressed as [32]

$$\begin{aligned}\mathcal{E}_c(\mathbf{R}) &= \frac{1}{2}\int_\Omega \left(\tilde{b}(\mathbf{x},\mathbf{R})+b(\mathbf{x},\mathbf{R})\right) V_c(\mathbf{x},\mathbf{R})\,\mathrm{d}\mathbf{x} + \frac{1}{2}\sum_J \int_\Omega b_J(\mathbf{x},\mathbf{R}_J)V_J(\mathbf{x},\mathbf{R}_J)\,\mathrm{d}\mathbf{x} \\ &\quad -\frac{1}{2}\sum_J \int_\Omega \tilde{b}_J(\mathbf{x},\mathbf{R}_J)\tilde{V}_J(\mathbf{x},\mathbf{R}_J)\,\mathrm{d}\mathbf{x}\,, \end{aligned} \tag{43}$$

where $V_c(\mathbf{x},\mathbf{R})$ is the solution of the Poisson equation

$$\frac{-1}{4\pi}\nabla^2 V_c(\mathbf{x},\mathbf{R}) = \tilde{b}(\mathbf{x},\mathbf{R}) - b(\mathbf{x},\mathbf{R}) \tag{44}$$

subject to periodic boundary conditions. The potential $V_c(\mathbf{x},\mathbf{R})$ so calculated is accurate to within a constant, which can be determined by evaluating $\sum_J (V_J(\mathbf{x},\mathbf{R}_J) - \tilde{V}_J(\mathbf{x},\mathbf{R}_J))$ at any point in space. Here, the 'reference' charge density $\tilde{b}(\mathbf{x},\mathbf{R})$ is the superposition of non-overlapping spherically symmetric and compactly supported 'reference' charge densities $\tilde{b}_J(\mathbf{x},\mathbf{R}_J) = -\frac{1}{4\pi}\nabla^2\tilde{V}_J(\mathbf{x},\mathbf{R}_J)$, i.e., $\tilde{b}(\mathbf{x},\mathbf{R}) = \sum_J \tilde{b}_J(\mathbf{x},\mathbf{R}_J)$. The correction to the forces on the nuclei can then be expressed as [32]

$$\begin{aligned}\mathbf{f}_I^c &= \frac{1}{2}\sum_{I'}\int_\Omega \Big[\nabla\tilde{b}_{I'}(\mathbf{x},\mathbf{R}_{I'})\left(V_c(\mathbf{x},\mathbf{R}) - \tilde{V}_{I'}(\mathbf{x},\mathbf{R}_{I'})\right) + \nabla b_{I'}(\mathbf{x},\mathbf{R}_{I'})\left(V_c(\mathbf{x},\mathbf{R}) + V_{I'}(\mathbf{x},\mathbf{R}_{I'})\right) \\ &\quad +\nabla V_{c,I'}(\mathbf{x},\mathbf{R}_{I'})\left(\tilde{b}(\mathbf{x},\mathbf{R}) + b(\mathbf{x},\mathbf{R})\right) + b_{I'}(\mathbf{x},\mathbf{R}_{I'})\nabla V_{I'}(\mathbf{x},\mathbf{R}_{I'}) - \tilde{b}_{I'}(\mathbf{x},\mathbf{R}_{I'})\nabla\tilde{V}_{I'}(\mathbf{x},\mathbf{R}_{I'})\Big]\,\mathrm{d}\mathbf{x}\,,\end{aligned}$$

where the summation index I' runs over the I^{th} atom and its periodic images, and

$$\nabla V_{c,I'}(\mathbf{x},\mathbf{R}_{I'}) = \nabla\tilde{V}_{I'}(\mathbf{x},\mathbf{R}_{I'}) - \nabla V_{I'}(\mathbf{x},\mathbf{R}_{I'}). \tag{45}$$

It is worth noting that the evaluation of the above energy and force corrections are also $\mathcal{O}(N)$. For the results presented in this work, we have chosen the 'reference' potential $\tilde{V}$ to be that employed previously in the context of all-electron electrostatics [59].

B. Formulation of the nonlocal pseudopotential force

The nonlocal pseudopotential component of the atomic force as presented in Eqn. 12 is

$$\mathbf{f}_I^{nl} = 2\mathrm{Tr}\left(\mathcal{D}^*\frac{\partial\mathcal{V}_{nl}}{\partial\mathbf{R}_I}\right). \tag{46}$$

Expanding the density operator and nonlocal pseudopotential operator:

$$\mathcal{D}^* = \sum_k g_k^* \left|\psi_k^*\right\rangle\left\langle\psi_k^*\right|, \tag{47}$$

$$\mathcal{V}_{nl} = \sum_I\sum_{lm}\gamma_l^I \left|\chi_{lm}^I\right\rangle\left\langle\chi_{lm}^I\right|, \tag{48}$$

the nonlocal pseudopotential force in Eqn. 46 can be written as

$$\begin{aligned}\mathbf{f}_I^{nl} &= 2\mathrm{Tr}\left(\sum_{lm}\sum_k \gamma_l^I g_k^* \left[|\frac{\partial\chi_{lm}^I}{\partial\mathbf{R}_I}\rangle\langle\chi_{lm}^I|\psi_k^*\rangle\langle\psi_k^*| + |\chi_{lm}^I\rangle\langle\frac{\partial\chi_{lm}^I}{\partial\mathbf{R}_I}|\psi_k^*\rangle\langle\psi_k^*|\right]\right) \\ &= 4\left(\sum_{lm}\sum_k \gamma_l^I g_k^* \langle\chi_{lm}^I|\psi_k^*\rangle\langle\psi_k^*|\frac{\partial\chi_{lm}^I}{\partial\mathbf{R}_I}\rangle\right) , \end{aligned} \tag{49}$$

where ψ_k^* are the ground-state orbitals, and g_k^* are the ground-state occupations. Rather than employ the above expression, we utilize a change of variables technique [60] to rewrite it as

$$\mathbf{f}_I^{nl} = 4\left(\sum_{lm}\sum_k \gamma_l^I g_k^* \langle\chi_{lm}^I|\psi_k^*\rangle\langle\nabla\psi_k^*|\chi_{lm}^I\rangle\right) = 4\mathrm{Tr}\left(\mathcal{V}_{nl}^I\mathcal{D}'\right) , \tag{50}$$

where

$$\mathcal{D}' = \sum_k g_k^* |\nabla\psi_k^*\rangle\langle\psi_k^*| . \tag{51}$$

We have found that the nonlocal pseudopotential force expression in Eqn. 50 results in significantly more accurate forces from a numerical standpoint compared to Eqn. 49. This is a consequence of the orbitals typically being smoother than the projectors.

References

[1] P. Hohenberg, W. Kohn, Physical Review 136 (1964) B864–B871.

[2] W. Kohn, L. J. Sham, Physical Review 140 (1965) A1133–A1138.

[3] J. E. Pask, B. M. Klein, C. Y. Fong, P. A. Sterne, Physical Review B 59 (1999) 12352–12358.

[4] R. Martin, Electronic Structure: Basic Theory and Practical methods, Cambridge University Press, 2004.

[5] P. Ciarlet, J. Lions, C. Le Bris, Handbook of Numerical Analysis : Special Volume: Computational Chemistry (Vol X), North-Holland, 2003.

[6] D. Marx, J. Hutter, Ab initio Molecular Dynamics: Basic Theory and Advanced Methods, Cambridge University Press, 2009.

[7] G. Kresse, J. Hafner, Physical Review B 47 (1993) 558.

[8] S. Goedecker, Rev. Mod. Phys. 71 (1999) 1085–1123.

[9] D. R. Bowler, T. Miyazaki, Reports on Progress in Physics 75 (2012) 036503.

[10] J. M. Soler, E. Artacho, J. D. Gale, A. Garcia, J. Junquera, P. Ordejon, D. Sanchez-Portal, J. Phys.: Condes. Matter 14 (2002) 2745–2779.

[11] SIESTA: www.icmab.es/siesta, accessed 2015-08-01.

[12] M. J. Gillan, D. R. Bowler, A. S. Torralba, T. Miyazaki, Comput. Phys. Commun. 177 (2007) 14–18.

[13] Conquest: www.order-n.org, accessed 2015-08-01.

[14] C. K. Skylaris, P. D. Haynes, A. A. Mostofi, M. C. Payne, J. Chem. Phys. 122 (2005).

[15] ONETEP: www.onetep.org, accessed 2015-08-01.

[16] E. Tsuchida, J. Phys. Soc. Jpn. 76 (2007).

[17] D. Osei-Kuffuor, J.-L. Fattebert, Phys. Rev. Lett. 112 (2014).

[18] S. Mohr, L. E. Ratcliff, P. Boulanger, L. Genovese, D. Caliste, T. Deutsch, S. Goedecker, J. Chem. Phys. 140 (2014).

[19] BigDFT: bigdft.org, accessed 2015-08-01.

[20] OpenMX: www.openmx-square.org, accessed 2015-08-01.

[21] N. Bock, M. Challacombe, C. K. Gan, G. Henkelman, K. Nemeth, A. M. N. Niklasson, A. Odell, E. Schwegler, C. J. Tymczak, V. Weber, FREEON, 2014. Los Alamos National Laboratory (LA-CC 01-2; LA-CC-04-086), Copyright University of California.

[22] FreeON: freeon.org, accessed 2015-08-01.

[23] A. Ruiz-Serrano, N. D. M. Hine, C.-K. Skylaris, J. Chem. Phys. 136 (2012).

[24] N. S. Bobbitt, G. Schofield, C. Lena, J. R. Chelikowsky, Phys. Chem. Chem. Phys. (2015). DOI: 10.1039/c5cp02561c.

[25] P. Suryanarayana, Chemical Physics Letters 584 (2013) 182–187.

[26] R. Haydock, V. Heine, M. Kelly, J Phys C Solid State 5 (1972) 2845.

[27] R. Haydock, V. Heine, M. Kelly, J Phys C Solid State 8 (1975) 2591–2605.

[28] S. Goedecker, L. Colombo, Physical Review Letters 73 (1994) 122.

[29] S. Goedecker, M. Teter, Physical Review B 51 (1995) 9455.

[30] A. Anantharaman, E. Cancès, Annales de l'Institut Henri Poincare (C) Non Linear Analysis 26 (2009) 2425–2455.

[31] L. Kleinman, D. Bylander, Physical Review Letters 48 (1982) 1425.

[32] S. Ghosh, P. Suryanarayana, arXiv preprint arXiv:1412.8250 (2014).

[33] P. Suryanarayana, V. Gavini, T. Blesgen, K. Bhattacharya, M. Ortiz, Journal of the Mechanics and Physics of Solids 58 (2010) 256 – 280.

[34] J. E. Pask, P. A. Sterne, Phys. Rev. B 71 (2005) 113101.

[35] P. Suryanarayana, K. Bhattacharya, M. Ortiz, Journal of the Mechanics and Physics of Solids 61 (2013) 38 – 60.

[36] S. Goedecker, Physical Review B 58 (1998) 3501.

[37] M. Benzi, P. Boito, N. Razouk, SIAM Review 55 (2013) 3–64.

[38] M. Alemany, M. Jain, L. Kronik, J. R. Chelikowsky, Physical Review B 69 (2004) 075101.

[39] A. Castro, H. Appel, M. Oliveira, C. A. Rozzi, X. Andrade, F. Lorenzen, M. A. L. Marques, E. K. U. Gross, A. Rubio, Physica Status Solidi B-Basic Solid State Physics 243 (2006) 2465–2488.

[40] H.-r. Fang, Y. Saad, Numerical Linear Algebra with Applications 16 (2009) 197–221.

[41] L. Lin, C. Yang, SIAM Journal on Scientific Computing 35 (2013) S277–S298.

[42] E. Prodan, W. Kohn, Proceedings of the National Academy of Sciences of the United States of America 102 (2005) 11635–11638.

[43] R. LeVeque, Finite Difference Methods for Ordinary and Partial Differential Equations: Steady-state and Time-Dependent Problems, SIAM, 2007.

[44] D. A. Mazziotti, Chemical Physics Letters 299 (1999) 473–480.

[45] D. Jordan, D. Mazziotti, The Journal of Chemical Physics 120 (2003) 574–578.

[46] P. Suryanarayana, D. Phanish, Journal of Computational Physics 275 (2014) 524 – 538.

[47] D. G. Anderson, Journal of the ACM (JACM) 12 (1965) 547–560.

[48] C. C. Paige, M. A. Saunders, SIAM journal on numerical analysis 12 (1975) 617–629.

[49] W. Hackbusch, Multi-grid methods and applications, volume 4, Springer Science & Business Media, 2013.

[50] C. J. Garcia-Cervera, J. Lu, Y. Xuan, W. E, Physical Review B 79 (2009) 115110.

[51] L. N. Trefethen, SIAM review 50 (2008) 67–87.

[52] W. L. Briggs, et al., The DFT: an owners' manual for the discrete Fourier transform, Siam, 1995.

[53] I. S. Dhillon, A New O n2 Algorithm for the Symmetric Tridiagonal Eigenvalue Eigenvector Problem, Ph.D. thesis, University of California, Berkeley, 1997.

[54] N. Troullier, J. L. Martins, Physical Review B 43 (1991) 1993–2006.

[55] J. P. Perdew, Y. Wang, Physical Review B 45 (1992) 13244.

[56] D. M. Ceperley, B. J. Alder, Phys. Rev. Lett. 45 (1980) 566–569.

[57] X. Gonze, J. M. Beuken, R. Caracas, F. Detraux, M. Fuchs, G. M. Rignanese, L. Sindic, M. Verstraete, G. Zerah, F. Jollet, M. Torrent, A. Roy, M. Mikami, P. Ghosez, J. Y. Raty, D. C. Allan, Computational Materials Science 25 (2002) 478–492(15).

[58] T. Ono, K. Hirose, Phys. Rev. Lett. 82 (1999) 5016–5019.

[59] J. E. Pask, N. Sukumar, S. E. Mousavi, International Journal for Multiscale Computational Engineering 10 (2012) 83–99.

[60] K. Hirose, T. Ono, Y. Fujimoto, S. Tsukamoto, First-principles calculations in real-space formalism, 2005.